

## The Use of Small Uncrewed Aircraft System Observations in Meteorological and Dispersion Modeling

FONG NGAN,<sup>a,b</sup> CHRISTOPHER P. LOUGHNER,<sup>a</sup> SONNY ZINN,<sup>a</sup> MARK COHEN,<sup>a</sup> TEMPLE R. LEE,<sup>c</sup> EDWARD DUMAS,<sup>c,d</sup> TRAVIS J. SCHUYLER,<sup>c,e</sup> C. BRUCE BAKER,<sup>c</sup> JOSEPH MALONEY,<sup>f</sup> DAVID HOTZ,<sup>f</sup> AND GEORGE MATHEWS<sup>f</sup>

<sup>a</sup> *Atmospheric Sciences Modeling Division, NOAA/Air Resources Laboratory, College Park, Maryland*

<sup>b</sup> *Cooperative Institute for Satellite Earth System Studies, College Park, Maryland*

<sup>c</sup> *Atmospheric Turbulence and Diffusion Division, NOAA/Air Resources Laboratory, Oak Ridge, Tennessee*

<sup>d</sup> *Oak Ridge Associated Universities, Oak Ridge, Tennessee*

<sup>e</sup> *Cooperative Institute for Severe and High-Impact Weather Research and Operations, Norman, Oklahoma*

<sup>f</sup> *Weather Forecast Office Morristown, NOAA/National Weather Service, Tennessee*

(Manuscript received 4 November 2022, in final form 27 February 2023, accepted 21 March 2023)


**ABSTRACT:** A series of meteorological measurements with a small uncrewed aircraft system (sUAS) was collected at Oliver Springs Airport in Tennessee. The sUAS provides a unique observing system capable of obtaining vertical profiles of meteorological data within the lowest few hundred meters of the boundary layer. The measurements benefit simulated plume predictions by providing more accurate meteorological data to a dispersion model. The sUAS profiles can be used directly to drive HYSPLIT dispersion simulations. When using sUAS data covering a small domain near a release and meteorological model fields covering a larger domain, simulated pollutants may be artificially increased or decreased near the domain boundary because of inconsistencies in the wind fields between the two meteorological inputs. Numerical experiments using the Weather Research and Forecasting (WRF) Model with observational nudging reveal that incorporating sUAS data improves simulated wind fields and can significantly affect mixing characteristics of the boundary layer, especially during the morning transition period of the planetary boundary layer. We conducted HYSPLIT dispersion simulations for hypothetical releases for three case study periods using WRF meteorological fields with and without assimilating sUAS measurements. The comparison of dispersion results on 15 and 16 December 2021 shows that using sUAS observational nudging is more significant under weak synoptic conditions than under strong influences from regional weather. Very different dispersion results were introduced by the meteorological fields used. The observational nudging produced not just an sUAS-nudged wind flow but also adjusted meteorological fields that further impacted the mixing calculation in HYSPLIT.

**KEYWORDS:** Dispersion; In situ atmospheric observations; Data assimilation; Model evaluation/performance; Boundary layer

### 1. Introduction

Small uncrewed aircraft systems (sUAS) have the unique ability to close a significant observation gap in the sampling of Earth's atmosphere because of their ability to obtain information on temperature, moisture, and wind in the lowest few hundred meters of the atmosphere (e.g., Holland et al. 2001; Houston et al. 2012; Elston et al. 2015). Over the past several years, both rotary-wing and fixed-wing sUAS have been used in field campaigns to study land-atmosphere interactions and planetary boundary layer (PBL) processes. Recent campaigns using sUAS have included, for example, the Verification of the Origins of Rotation in Tornadoes Experiment-Southeast (VORTEX-SE; e.g., Lee et al. 2019; Wagner et al. 2019) in

northern Alabama, the Land-Atmosphere Feedback Experiment (LAFE; e.g., Wulfmeyer et al. 2018, 2023) in northern Oklahoma, studies of the North American eclipse on 21 August 2017 (e.g., Bailey et al. 2019; Buban et al. 2019), the Lower Atmospheric Process Studies at Elevation-A Remotely Piloted Aircraft Team Experiment (LAPSE-RATE; e.g., Barbieri et al. 2019; de Boer et al. 2020a,b) in Colorado, and the Chequamegon Heterogeneous Ecosystem Energy-Balance Study Enabled by a High-Density Extensive Array of Detectors 2019 (CHEESEHEAD19; e.g., Butterworth et al. 2021) in Wisconsin. Since 2015, the NOAA Air Resources Laboratory (ARL) has been using a fleet of sUAS to sample the PBL. ARL's sUAS measurements include vertical profiles of thermodynamic and kinematic parameters and can also be used to infer fluxes near the surface (Lee et al. 2017; Buban et al. 2019; Lee et al. 2019). From August through December 2020, ARL performed quasi-routine flights with its Meteomatics Meteodrone SSE sUAS at the Oliver Springs Airport (OSI) in Oliver Springs, Tennessee. The Meteomatics Meteodrone is a rotary-wing hexacopter sUAS. Its payload includes a bead thermistor and capacitive sensor for sampling temperature and relative humidity, respectively, and a piezo resistive pressure sensor. Although there is no sensor package on the aircraft explicitly used

 Denotes content that is immediately available upon publication as open access.

Baker's current affiliation: Retired.

Corresponding author: Fong Ngan, fantine.ngan@noaa.gov

DOI: 10.1175/JAMC-D-22-0182.1

© 2023 American Meteorological Society. This published article is licensed under the terms of the default AMS reuse license. For information regarding reuse of this content and general copyright information, consult the AMS Copyright Policy ([www.ametsoc.org/PUBSReuseLicenses](http://www.ametsoc.org/PUBSReuseLicenses)).

for sampling wind, wind speed and wind direction are derived from the Meteomatics Meteodrone using global positioning system (GPS) and onboard inertial sensors (Dumas et al. 2021). Because the sUAS can provide a unique observing system capable for the vertical profiles of meteorological conditions within the PBL, using the data in dispersion modeling may be beneficial for improving plume prediction by providing more accurate meteorological variables.

Recent studies demonstrated the potential value of using sUAS measurements in numerical weather prediction for reducing model biases and providing better forecasts during various high-impact weather events (Flagg et al. 2018; Leuenberger et al. 2020; Jensen et al. 2021). The Advanced Research dynamic core of the Weather Research and Forecasting (WRF) Model (Powers et al. 2017) has been frequently used to generate meteorological input fields for dispersion applications (Hegarty et al. 2013; Ngan and Stein 2017; Chai et al. 2018; Loughner et al. 2021). Jensen et al. (2021, 2022) assessed the benefit of assimilating sUAS observations in WRF simulations for a case study of drainage and up-valley flow in complex terrain. The sUAS-improved meteorological input fields may further positively impact air quality and dispersion modeling. The NOAA/ARL HYSPLIT model (Stein et al. 2015; Draxler et al. 2022) is one of the most extensively used atmospheric transport and dispersion models in the atmospheric sciences community, including widespread operational emergency-response applications to assess the movement of harmful materials in the atmosphere. One of the sources of uncertainty in dispersion modeling is the accuracy of the meteorological input used to drive the model. Because most emissions start at or near the surface, sUAS measurements from the lowest part of the PBL can be significant in helping to improve the overall quality of the dispersion prediction.

The objective of this study is to explore different ways of using the sUAS-collected meteorological data in numerical modeling and to assess their impact on meteorological and dispersion simulations. The meteorological profiles taken by the Meteomatics Meteodrone SSE sUAS may be used directly to drive HYSPLIT simulations after converting the data to the HYSPLIT meteorological input file format. However, profiles in one location can only provide a limited area of gridded data for running trajectory and dispersion simulations. For this reason, it is better to profile simultaneously using multiple sUAS (e.g., Nolan et al. 2018). The second approach is to use the converted sUAS data with other Numerical Weather Prediction (NWP) products as inputs into HYSPLIT simulations. One of the available products that can provide forecast and near real-time meteorological data is NOAA's High-Resolution Rapid Refresh (HRRR) model (Benjamin et al. 2016). The inconsistency of model winds between the sUAS observations and NWP models may cause an issue as HYSPLIT simulates the plume across the inner data domain generated from the sUAS observations to the outer domain based on an NWP model. Another alternative is assimilating the sUAS data within an NWP model (such as WRF) simulation to improve the accuracy of the model's predicted kinematic and thermodynamic fields. Using the sUAS-assimilated WRF fields to drive HYSPLIT simulations, we

assessed how the sUAS data impacts the model's performance in simulating wind fields and its impacts on the transport and mixing of pollutants.

Four-dimensional data assimilation (so-called nudging) is a well-known and efficient method in WRF to reduce model bias by incorporating observations during the simulation (Deng et al. 2009; Reen 2016). The model considers gridded analysis fields (analysis nudging) or individual observations (observational nudging) and corrects biases for temperature, moisture, and  $u$  and  $v$  components of wind at each integration time step. The nudging tool in WRF has been widely used and has been demonstrated to be beneficial in generating improved meteorological input data for air quality applications and dispersion modeling (Hegarty et al. 2013; Ngan et al. 2015; Li et al. 2016; Lucas et al. 2017; Tran et al. 2018; Tomasi et al. 2019; Jia et al. 2021; Abida et al. 2022). Most previous studies used conventional hourly observations, such as surface measurements at airports and radiosondes. In this study, temperature and wind data measured by the sUAS were ingested into WRF simulations using the observational nudging technique to adjust the model prediction toward sUAS measurements. Profiles every 30 min of the lowest several hundred meters above ground level (AGL) were used in this work. Then, HYSPLIT simulations were conducted using the nudged WRF fields. The results are compared with runs driven by the meteorological fields from the HRRR model and a nonnudged WRF simulation. We applied this method and comparison to three study periods to understand the impact of using sUAS wind and temperature profiles in WRF simulations through observational nudging and its associated impacts on HYSPLIT simulations. Section 2 presents a brief overview of the observational datasets, including the sUAS and tower data used in this study. Model configurations for WRF and HYSPLIT are described in section 3. Section 4 presents the results and discussions for the three case studies, and section 5 provides a summary and a discussion of future work.

## 2. Observational data

### a. sUAS observations

#### 1) CALIBRATIONS OF ONBOARD SUAS SENSORS

All sUAS flights were conducted using a Meteomatics Meteodrone SSE (e.g., Koch et al. 2018), which weighs 0.7 kg and has a 0.4-m wingspan. The onboard temperature and humidity sensors have reported accuracies of  $\pm 0.1^\circ\text{C}$  and  $< 2\%$ , respectively, and response times of  $< 1$  and  $< 4$  s, respectively, whereas pressure is accurate to within  $\pm 0.1$  hPa. Prior to being deployed on the sUAS and following the procedure described by, for example, Lee et al. (2019), the thermodynamic sensors were calibrated using ATDD's National Institutes for Standards and Technology traceable calibration chamber using three temperature set points ( $10^\circ$ ,  $20^\circ$ , and  $30^\circ\text{C}$ ) and five relative humidity set points (20%, 40%, 60%, 80%, and 94%). These tests indicated that the thermodynamic sensors have a cold and dry bias. The cold bias was as large as  $0.3^\circ\text{C}$ , whereas the dry bias ranged from 2% for low relative humidity to  $\sim 9\%$  for high relative humidity. Although we ourselves

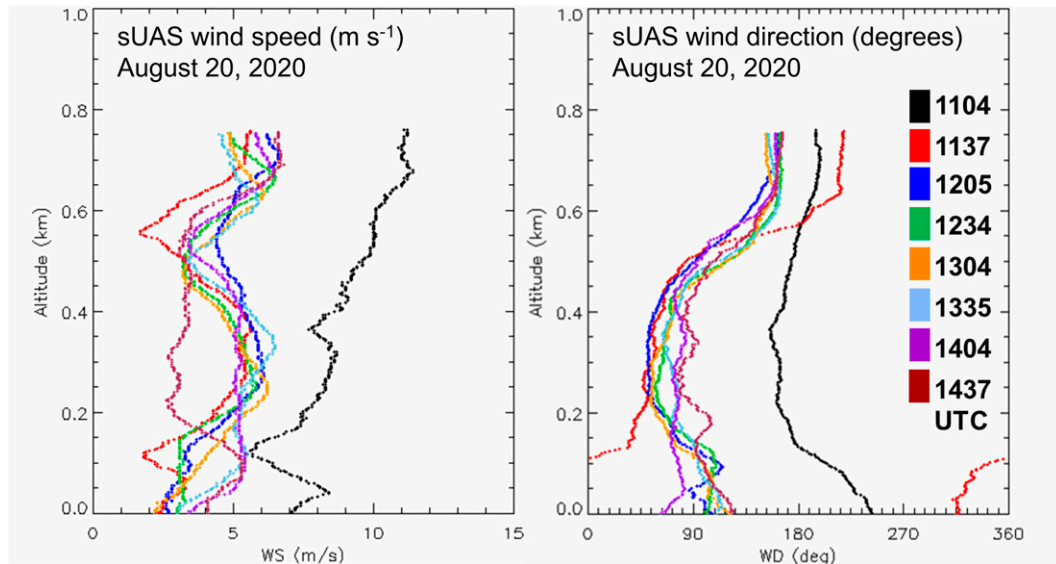


FIG. 1. Wind (left) speed and (right) direction profiles measured by a Meteomatics Meteodrone SSE small UAS on 20 Aug 2020 from OSI (36.0371°N, 84.3078°W).

did not calibrate wind measurements from the Meteomatics Meteodrone, previous work by Koch et al. (2018) reported small biases in the wind measurements, that is, a  $+0.2 \text{ m s}^{-1}$  wind speed bias and clockwise  $7^\circ$  wind direction bias.

## 2) sUAS FLIGHTS

Between 20 August and 10 December 2020, NOAA/ARL conducted 241 UAS flights spanning 31 days using its Meteodrone SSE sUAS. The profiling location was at OSI in Oliver Springs (36.0371°N, 84.3078°W; 240 m above mean sea level), which is about 5 km northwest of Oak Ridge, Tennessee, and 35 km northwest of Knoxville, Tennessee. Although OSI is relatively flat and consists of a grassy runway available for use by full-scale aircraft, the area surrounding the site consists of complex topography. 100-m forested ridgetops immediately surround the site;  $>1000\text{-m}$  mountains of the Cumberland Plateau are located north and west of the site, whereas the Smoky Mountains with maximum ridgetop heights of up to 2000 m are located south and east of OSI (Fig. 2). The winds induced by these terrain features (e.g., local drainage winds) cannot be resolved well by NWP models; the use of sUAS observations helps in this regard and is the major focus of this study.

At OSI, ARL operated under the following Certificates of Authorization (COA) from the Federal Aviation Administration (FAA): 2019-ESA-3583-COA and 2021-ESA-8968-COA. These COAs enabled flights up to 1067 m AGL. Two of the authors on this work, Dr. Schuyler and Mr. Dumas, are certified as remote pilots for sUAS by the FAA under Part 107, received manufacturer training on the sUAS platform, and served as pilots in command (PIC) for this work.

Flights at OSI were conducted beginning around sunrise and continuing at 30-min intervals until 3.5–4 h after sunrise. Per ARL's COA with the FAA, the sUAS was permitted to

collect vertical profiles up to a maximum altitude of 1000 m AGL; however, the sUAS PIC and visual observer had to maintain visual line of sight of the sUAS with the unaided eye throughout the entire profile. Thus, the aircraft was flown by the PIC to the maximum altitude that both the PIC and the visual observer could safely see the aircraft and then brought down. The sky conditions and local visibility determined the maximum altitude attainable on each flight, and although the strobes and lights provided sufficient visibility to be seen at 1000 m AGL on some days, not every flight was able to be flown to 1000 m AGL because of variable lighting and visibility conditions. The sUAS ascended/descended at a vertical velocity of  $3 \text{ m s}^{-1}$ ; thus, the typical flight duration was 10–12 min. Temperature, pressure, humidity, and wind measurements from these flights were provided in near-real time to support short-term weather forecasting operations at the National Weather Service (NWS) Weather Forecast Office (WFO) in Morristown, Tennessee, and to study the early-morning transition period of the PBL (Dumas et al. 2021). Figure 1 shows the sUAS wind speed and direction profiles taken on 20 August 2020. The observational data are available during 1104–1437 UTC in 30-min intervals, from the surface up to nearly 800 m AGL. A significant change of wind direction, from southwesterly to northwesterly and then easterly, was observed within the lowest 100 m AGL during 1100–1200 UTC. The wind speed was larger ( $5\text{--}10 \text{ m s}^{-1}$ ) during the first flight at 1104 UTC and then lessened (ranging from 2 to  $5 \text{ m s}^{-1}$ ) for the other seven flights.

### b. Tower observations

For the evaluation of the WRF results, in addition to the sUAS profiles, we used meteorological observations taken at OSI and Knox County Radio Control Society, Inc. (KCRC), located about 12 km southeast of OSI (Fig. 2). At OSI, wind

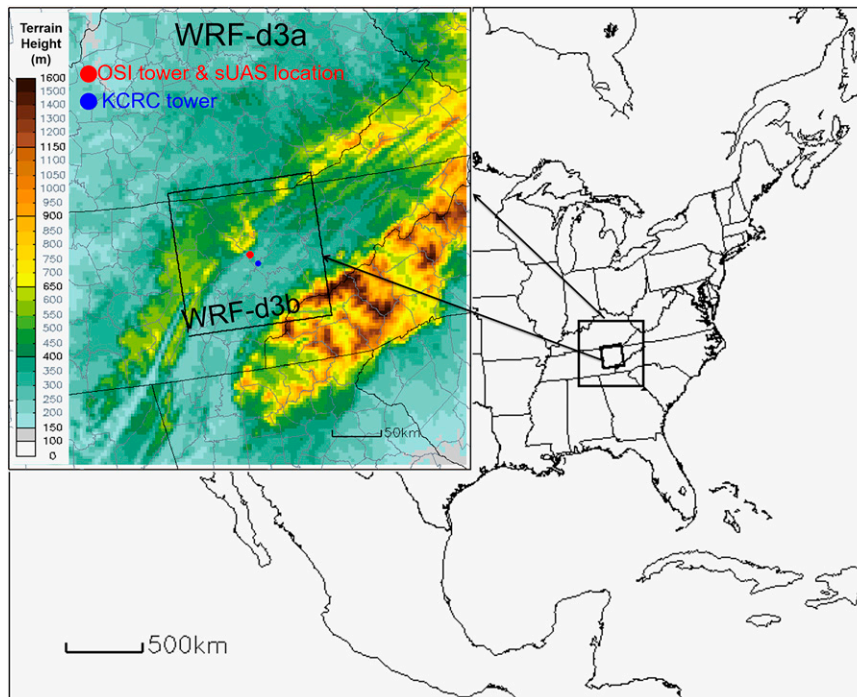


FIG. 2. WRF simulation domains, terrain height from WRF, sUAS profiling location, and two meteorological tower sites: OSI (36.0371°N, 84.3078°W) and KCRC (35.9480°N, 84.2332°W).

speed and direction were sampled at 5.8 m AGL using an R.M. Young Company 05103 anemometer, and air temperature was sampled using a Thermometrics Corp. PRT installed at 5.2 m AGL (Dumas et al. 2021). The measurements at KCRC included an R.M. Young 05103 anemometer for wind speed and direction at 4.4 m AGL, and a Thermometrics PRT at 2.8 m AGL for temperature. The tower data were reported every 10 s and were aggregated to 10-min averages for comparison with the WRF Model results.

### 3. Modeling method

#### a. Using sUAS data in WRF and HYSPLIT

HYSPLIT requires gridded meteorological data at multiple heights and time periods over the duration of the simulation. To use the sUAS data to directly drive HYSPLIT, we developed a utility to create a combined profile of meteorological fields from the sUAS measurements from the surface to the top of the profile. This was coupled with archived HYSPLIT meteorological input files above the sUAS flight to create a new set of meteorological input files for running HYSPLIT. For this study, profiles from HRRR meteorological files were appended to the top of sUAS profiles to create the sUAS-based HYSPLIT meteorological input files. This utility was configured so the profiles will be used within a 20 km × 20 km area surrounding the sUAS measurement site, although it is understood that the sUAS profile at one location would not necessarily be representative of conditions throughout even this limited domain. Considering a 3 m s<sup>-1</sup> wind speed

condition, a plume travels about 10 km from the source location within an hour. Thus, the gridded data based on one sUAS profile used in this way generally only provide the meteorological conditions for a relatively small area to drive HYSPLIT. For simulation of a plume traveling beyond the assumed domain of the sUAS observations, we used the HRRR meteorological fields to continue the dispersion simulation. An issue associated with this approach is that a discontinuity may happen when the model plume crosses over the boundary between the converted-sUAS inner domain and HRRR outer domain. Thus, we incorporated the sUAS data in WRF simulations through observational nudging to generate improved, continuous meteorological fields for the use of dispersion modeling. In this study, we used a meteorological model with a horizontal spatial resolution of 3 km to drive the HYSPLIT model, and a HYSPLIT concentration grid output resolution of 1 km over which the concentrations were calculated by summing up the computational “particles” in each grid cell. The model output frequency was at 30-min intervals for WRF and 10-min intervals for HYSPLIT. Such resolution is reasonable for mesoscale atmospheric phenomena and short-range transport and dispersion scenarios, as long as the terrain is not overly complex.

We selected two retrospective cases (Table 1), a single day in August (case 1) and three consecutive days in November (case 2), to test the use of sUAS data in WRF modeling and optimize the nudging configuration. A third case testing the capability in an operational setting was also carried out (Table 1). HYSPLIT simulations were driven by the WRF Model output with and without using the sUAS data. By comparing the



TABLE 1. List of cases and available sUAS profiles in this study.

	Date	No. of profiles	Profile time (UTC)
Case 1 (retrospective run)	20 Aug 2020	8	1104, 1137, 1205, 1234, 1304, 1335, 1404, 1437
Case 2 (retrospective run)	16 Nov 2020	8	1249, 1320, 1349, 1449, 1450, 1520, 1550, 1619
	17 Nov 2020	8	1249, 1319, 1349, 1420, 1449, 1519, 1550, 1619
	18 Nov 2020	8	1249, 1319, 1349, 1420, 1449, 1520, 1549, 1619
Case 3 (operational run)	15 Dec 2021	8	1303, 1335, 1405, 1435, 1505, 1535, 1607, 1635
	16 Dec 2021	8	1306, 1331, 1405, 1435, 1504, 1534, 1604, 1634

results, we assessed the impact of using nudged-WRF fields on dispersion simulations.

Assimilating meteorological data collected via sUAS into WRF has the potential to benefit retrospective cases and enhance the HYSPLIT emergency response operations, including the use of HYSPLIT by NOAA Weather Forecast Office and within the Real-time Environmental Applications and Display System (READY; Rolph et al. 2017). The automated sUAS data ingestion feature was added to READY to incorporate sUAS data files and assimilate them with the WRF Model. This prototype system demonstrates how the meteorological fields converted directly from sUAS or WRF simulations assimilated with sUAS measurements can be used to drive HYSPLIT for transport and dispersion simulations to support emergency response to hypothetical and real hazardous air pollution events. An end-to-end system was developed to automatically ingest and assimilate sUAS profile data into the READY system for emergency-response HYSPLIT simulations, and this system was tested during the sUAS flights conducted on 15 and 16 December 2021 (case 3).

*b. WRF Model configuration*

The Advanced Research version of the WRF Model, version 4.2.2, was used to generate the meteorological input fields to drive HYSPLIT. As shown in Fig. 2, we configured two sets of independent domains with a horizontal grid spacing of 3 km. The domain labeled as WRF-d3a was for retrospective runs (i.e., case 1 and 2), whereas the smaller domain labeled as WRF-d3b was for operational use (i.e., case 3). We used 33 vertical layers with higher vertical resolution near the surface and coarser resolution near the top of the model domain at 100 hPa. There were 20 layers below 850 hPa (~1.5 km), with the first midlayer height of the model at around 8 m. The retrospective simulations were initialized using the NCEP Final (FNL) Operational Model Global Tropospheric Analyses

(NCEP/NWS/NOAA/U.S. Department of Commerce 2000) in 1° spatial resolution and available every 6 h. For the operational run, the model was initialized using the North American Mesoscale Forecast System (NAM) in 12-km grid spacing, downloaded from the NOAA Operational Model Archive and Distribution System (NOMADS; Rutledge et al. 2006). The physics options used for the WRF simulations include the Rapid Radiative Transfer Model for GCMs for radiation parameterization (RRTMG; Iacono et al. 2008), WSM6 for microphysics (Lim and Hong 2010), the Grell 3D ensemble for the subgrid cloud scheme (Grell and Devenyi 2002), the Noah land surface model (Chen and Dudhia 2001), the Monin–Obukhov surface scheme, and the Shin–Hong PBL parameterization scheme (Shin and Hong 2015).

It is a common practice to use the nudging feature in WRF to provide more accurate meteorological input fields to drive air quality and dispersion models (Hegarty et al. 2013; Ngan et al. 2015; Li et al. 2016; Lucas et al. 2017; Tran et al. 2018; Tomasi et al. 2019; Jia et al. 2021; Abida et al. 2022). A first set of WRF simulations was carried out as described above without observational nudging, and a second set of simulations was performed using observational nudging with sUAS profiles to minimize the bias of wind and temperature prediction. The sUAS data was provided as ASCII format files generated by Meteomatics software for the measurements taken during the ascending portions of the sUAS flights. We converted the observational files to the format required by WRF’s observational nudging. The variables for the observational nudging were temperature, relative humidity, and the *u* and *v* wind components. Profile data collected via sUAS were inserted into WRF from the surface to the top of the profile at vertical intervals of 5 hPa. Sensitivity tests were performed and evaluated with sUAS profiles to find an observational nudging configuration to maximize the influence of the sUAS data (Table 2 and section 4a). The WRF nudging parameters

TABLE 2. MAE computed using sUAS-collected data on 20 Aug 2020 for temperature (°C), wind speed (m s<sup>-1</sup>), and wind direction (°). Run 1: WRF simulation without observational nudging. Runs 2–6: WRF sensitivity tests with sUAS profiles nudging. Observational nudging parameters including *twindo*—the half-period time window for using observations (h), *coef\_wind*—the nudging coefficient of wind (s<sup>-1</sup>), and *coef\_t*—the nudging coefficient of temperature (s<sup>-1</sup>).

Case name	Case description	<i>T</i>	WS	WD
Run 1	Control run (“nonnudged WRF” hereinafter)	1.862	2.483	37.161
Run 2	sUAS obs nudging: <i>twindo</i> = 1	0.643	1.326	65.923
Run 3	Shorten obs time window: <i>twindo</i> = 0.4	0.633	1.415	30.599
Run 4	Increase wind coef: <i>coef_wind</i> = 3.2 × 10 <sup>-3</sup>	0.615	0.833	24.795
Run 5	Increase temperature coef: <i>coef_t</i> = 1.2 × 10 <sup>-3</sup>	0.536	0.864	27.952
Run 6	Insert sUAS 5-hPa (10 hPa for other runs) vertical interval (“Nudged WRF” hereinafter)	0.463	0.758	14.370

were set as following: 1) 0.4 h for the half-period time window for using observations (*twindo*), 2)  $3.2 \times 10^{-3} \text{ s}^{-1}$  for the nudging coefficient of wind (*coef\_wind*), 3)  $1.2 \times 10^{-3} \text{ s}^{-1}$  for the nudging coefficient of temperature (*coef\_t*), 4)  $8.0 \times 10^{-4} \text{ s}^{-1}$  for the nudging coefficient of relative humidity (*coef\_mois*), and 5) 20 km for the horizontal radius of influence (*rinxy*).

### c. HYSPLIT configuration

We conducted HYSPLIT simulations for hypothetical releases to study the impact of the various sUAS meteorological products on HYSPLIT performance using different meteorological datasets: 1) sUAS-HRRR single profile, 2) sUAS-HRRR single profile with a HRRR outer nest, 3) HRRR, 4) nonnudged WRF, and 5) nudged WRF. The HYSPLIT simulations started at 1130 UTC (case 1) or 1300 UTC (case 2 and case 3), corresponding to the times when the sUAS nudging started in the WRF simulations. We used a unit emission ( $1 \text{ g h}^{-1}$ ) for a continuous release at 10 m AGL with 50 000 particles total for 3 h. The release location was at OSI ( $36.0371^\circ\text{N}$ ,  $-84.3078^\circ\text{W}$ ) and coincident with the sUAS profiling location. The concentrations were calculated on a  $0.01^\circ \times 0.01^\circ$  ( $\sim 1 \text{ km} \times 1 \text{ km}$ ) horizontal grid in a layer 0–100 m above the ground using 10-min temporal averaging. The HYSPLIT simulations utilized the Kantha–Clayson turbulent mixing scheme, which uses the friction velocity, boundary layer depth, and other state variables from WRF to compute the turbulent velocity variances for the dispersion calculation (Ngan et al. 2019).

## 4. Results and discussions

### a. Case 1–20 August 2020

Eight sUAS profiles during 1104–1437 UTC 20 August 2020 were ingested into the WRF simulation. The choice of parameters for the nudging determines the strength of adjustment made on model calculations toward observations. We conducted nudged simulations with different settings and found a nudging configuration with the smallest temperature and wind bias as measured by the comparison with sUAS profiles. The mean absolute error (MAE) for all nudging runs (runs 2–6 in Table 2) was significantly smaller than the nonnudged run (run 1). Using a smaller temporal weighting parameter (*twindo* = 0.4 h in run 3), the half-period time window for nudging, reduced wind direction errors. When increasing the nudging weight for wind (*coef\_wind* =  $3.2 \times 10^{-3} \text{ s}^{-1}$  in run 4) and temperature (*coef\_t* =  $1.2 \times 10^{-3} \text{ s}^{-1}$  in run 5), the results had lower wind speed and direction MAE and temperature MAE, respectively. We also tested using the sUAS profile with different vertical pressure intervals. The 5-hPa interval (run 6) gave a better result statistically than the one using 10-hPa interval (run 5). Thus, the nudging configuration of run 6 was applied to case 2 and 3 presented in sections 4b and 4c. It is understood that these findings applied to this specific study and are not necessarily general. Additional sensitivity tests will be needed if sUAS profiling is carried out at different geographic locations, under different weather conditions, and/or with different temporal and spatial availability. However, the parameters used in this study can be an initial setting for

other WRF simulations with sUAS data observational nudging. Note that we set the horizontal radius of influence to 20 km in the observational nudging as the sUAS data were converted to a  $20 \text{ km} \times 20 \text{ km}$  area meteorological fields for driving HYSPLIT if WRF was not run. The choice is arbitrary, but it will certainly affect the nudged simulation results. Additional research and sensitivity analyses will need to be conducted to examine the influence of the horizontal radius of influence on the accuracy of the nudged simulations.

The comparison of observed and modeled profiles for wind speed, wind direction, and temperature shows that the observational nudging successfully adjusted the predicted wind and temperature toward the measurements taken by the sUAS (Fig. 3). At 1100 UTC (0700 local time), the easterly winds in the run without observational nudging were corrected, and the wind directions in the nudged run were well simulated. The wind speed and temperature underprediction were still present, even with the observational nudging. However, their variations along with altitude in the nudged run matched better with the sUAS profiles than in the nonnudged run. As the nudging coefficient for moisture was small, we expected the nonnudged and nudged predicted similar relative humidity as shown in Fig. 3. The evaluation for the rest of this study focused on the wind speed and direction because they directly drive the transport and dispersion of particles in the model. However, we hope to put more effort in a future study to evaluate the nudged temperature and moisture and the associated influence on dispersion simulations. In the late-morning hours (1300 UTC and later), we notice smaller differences between the nonnudged and nudged wind directions than earlier that morning (1100 UTC). During the morning transition, the PBL evolves from nighttime to daytime, and it can be challenging for meteorological models to simulate accurate wind patterns and mixing characteristics. For this reason, experimental and numerical studies (e.g., Wildmann et al. 2015; Dimitrova et al. 2016; Efstathiou et al. 2016; Cuchiara and Rappengluck 2019; Bauer et al. 2020, and Nielsen and Rahn 2022) were conducted to understand the growth of the convective boundary layer from the stable nocturnal boundary layer. Cuchiara and Rappengluck (2019) argued that the morning transition of PBL is important for the vertical mixing of pollutants not only because of emissions from the surface but also because of pollutants from the previous day stored within the residual layer. The uncertainty in the meteorological input may cause errors in modeling the transport and dispersion of pollutants. The nudging approach using observations, such as sUAS measurements, can be a remedy to model deficiencies under this challenging condition.

Figure 4 is the spatial plot of the model wind fields, showing the influence of the sUAS data in the WRF simulation through observational nudging. Larger wind speeds and more easterly components of wind direction were simulated in the nudged case around OSI. By setting 20 km around the sUAS launch location for the radius of influence for the observational nudging, the impact of sUAS profiles on the WRF prediction was present at the KCRC station. Note that the KCRC tower data were not included in the WRF simulation.

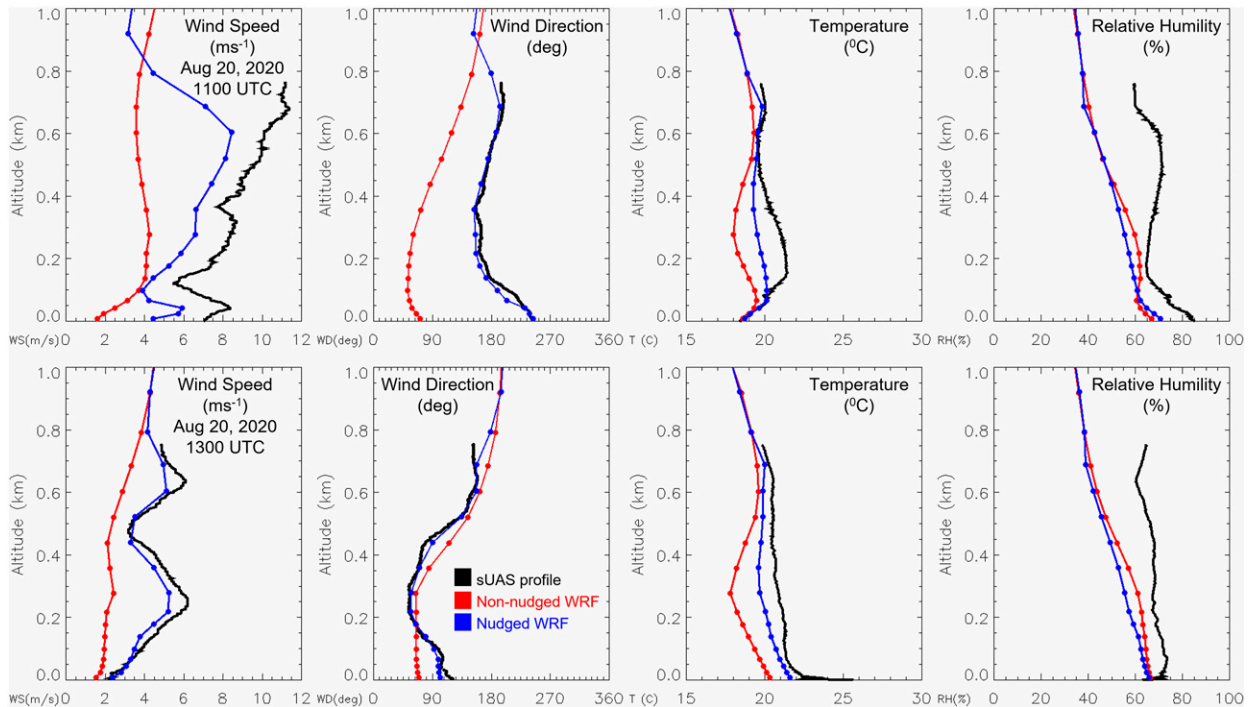


FIG. 3. The observed and WRF-modeled (left) wind speed, (left center) wind direction, (right center) temperature, and (right) relative humidity profiles at (top) 1100 UTC and (bottom) 1300 UTC 20 Aug 2020. The y axis is altitude (km AGL).

As soon as the observational nudging started, the positive wind speed bias was reduced, and the wind direction was adjusted closer to the KCRC measurement (Fig. 5). In later hours, the sUAS nudging changed the negative wind speed bias in the nonnudged run to a positive bias while improving the wind direction prediction. For temperature and PBL height, the nudging had a minor impact, as shown in the

comparison at the KCRC tower. The meteorological measurements collected at two towers were not included in WRF’s observational nudging but served as an independent dataset to evaluate the meteorological fields, allowing us to assess how much the nudging with sUAS profiles changed (improved or degraded) the wind and temperature predictions as compared with the surface observations.

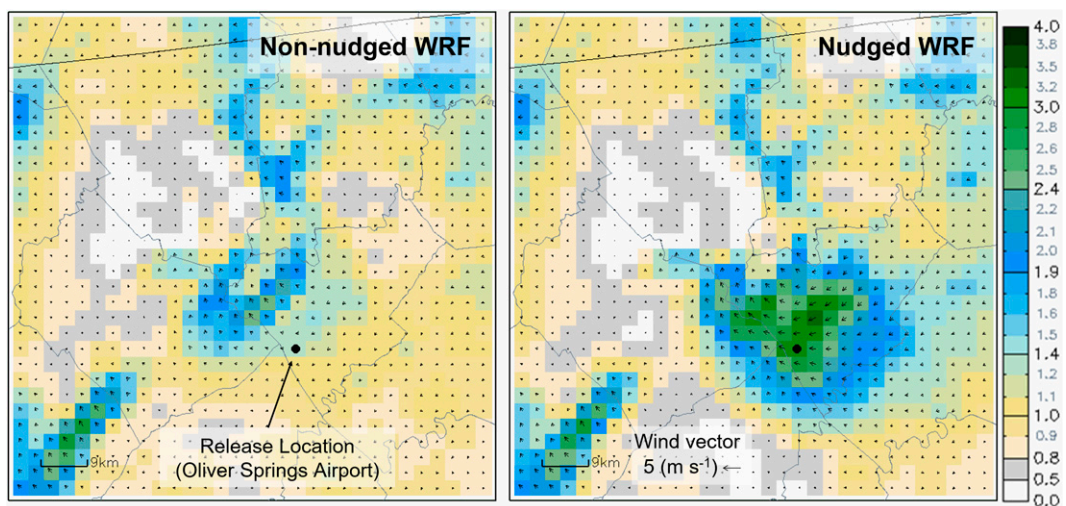


FIG. 4. Horizontal distribution of wind speed and wind vector from two WRF simulations, (left) without observational nudging and (right) with observational nudging using sUAS data, at 1330 UTC 20 Aug 2020 ( $m s^{-1}$ ). The black dot indicates the HYSPLIT plume release location and the sUAS profiling location.

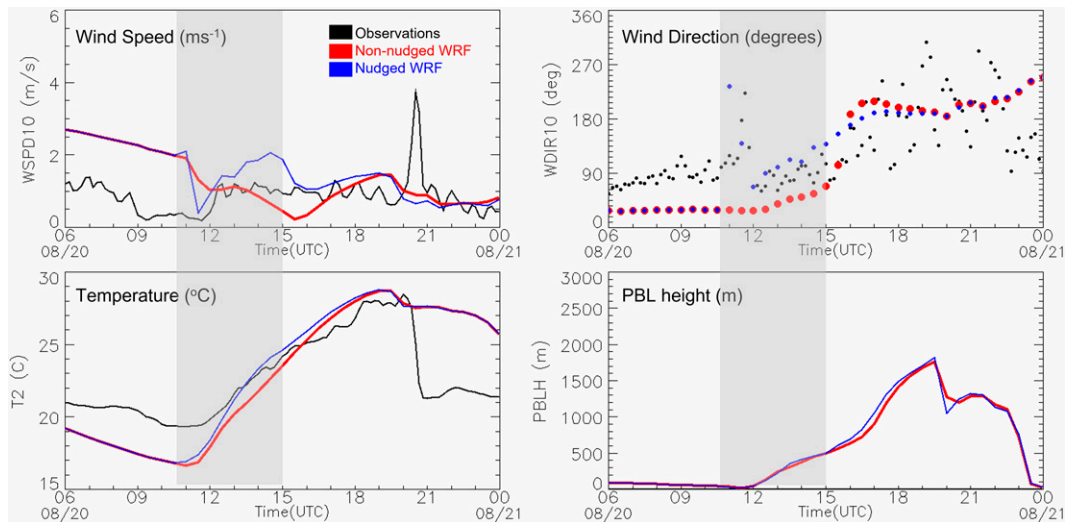


FIG. 5. Time series of observed and modeled (top left) wind speed, (top right) wind direction, (bottom left) temperature, and (bottom right) PBL height (no observation) at KCRC. The sUAS observational nudging was carried out during the gray-shaded time periods.

Five HYSPLIT simulations were conducted using the following meteorological input fields: 1) sUAS-HRRR single profile, 2) sUAS-HRRR profile for an inner domain with HRRR model fields for an outer domain, 3) HRRR model fields only, 4) nonnudged WRF, and 5) nudged WRF with the sUAS-data observational nudging. A 3-h hypothetical release using a unit emission ( $1 \text{ g h}^{-1}$ ) was set at OSI ( $36.0371^\circ\text{N}$ ,  $-84.3078^\circ\text{W}$ ) and 10 m AGL with 50 000 computational particles. The concentration was calculated by summing particles in the volume of  $1 \text{ km} \times 1 \text{ km}$  and from the surface to 100 m AGL with 10-min temporal averaging. The concentration plots at 1330 UTC (i.e., 2 h after the initiation) are shown in Fig. 6. The simulation using the sUAS-HRRR single profile produces a realistic plume downwind of a source. However, in this case, one observed profile only covers a limited area, such as a 20 km by 20 km domain. By the second hour of the run, the model plume hit the western boundary of the data domain, and no meteorological data were available beyond the boundary for HYSPLIT to continue the simulation. The model plume could travel farther away when using HRRR model fields for the outer nest together with the converted-sUAS measurements. However, pollutant concentrations can be artificially affected at the domain boundary area due to the inconsistency of winds between the two datasets; in this case, the pollutant concentration appears to be artificially enhanced due to lower wind speeds at the boundary in the HRRR-based outer domain than with the sUAS inner domain. By assimilating the sUAS observations into WRF, we can avoid the issue of the limited domain and the flow inconsistency of combining the sUAS dataset and other NWP products. In the HRRR and nonnudged WRF meteorological inputs, weaker wind speeds resulted in higher pollutant concentrations near the source location (Fig. 6, bottom panel). Both plumes went in the southwest direction and had similar horizontal coverage. Using the nudged WRF meteorological fields, the model

plume moved westward and later curved northward when going farther away from the source location. This case study demonstrates that using sUAS wind and temperature profiles in WRF simulations through observational nudging can reduce WRF Model biases and impact HYSPLIT dispersion simulations.

#### b. Case 2–16–18 November 2020

We applied sUAS nudging to the WRF Model for a 3-day period from 16 to 18 November 2020. There were eight sUAS profiles each day starting at 1249 UTC. The sUAS profile evaluation continues to show that the observational nudging approach positively impacted wind prediction. The improvement of wind direction was especially evident on 16 and 17 November (Fig. 7). In addition to comparing the vertical profiles, we used tower measurements taken at OSI for the model evaluation. The tower data were not included in WRF simulations and were taken at the site where the sUAS flights took place. Figure 8 shows the time series of surface wind speed and direction from the nonnudged WRF, nudged WRF, and HRRR meteorological fields. The wind prediction was adjusted in the nudged case during the hours when sUAS profiles were available (shaded areas in Fig. 8). The nudged wind directions on 16 and 17 November had a better agreement with the tower wind measurements. At the end of sUAS profiling periods, the influence of observational nudging on the model wind direction lasted a little longer, up to about an hour on 16 November. Then, the model winds returned to the nonnudged conditions (outside the gray-shaded areas in Fig. 8). This demonstrates the usefulness of the sUAS profiles in correcting wind direction errors through observational nudging. Dispersion simulations may better simulate the plume movement by using the nudged wind fields while, outside the sUAS profile period, the dispersion results may inherit the errors in the model wind fields that drive the simulations. On 18 November,



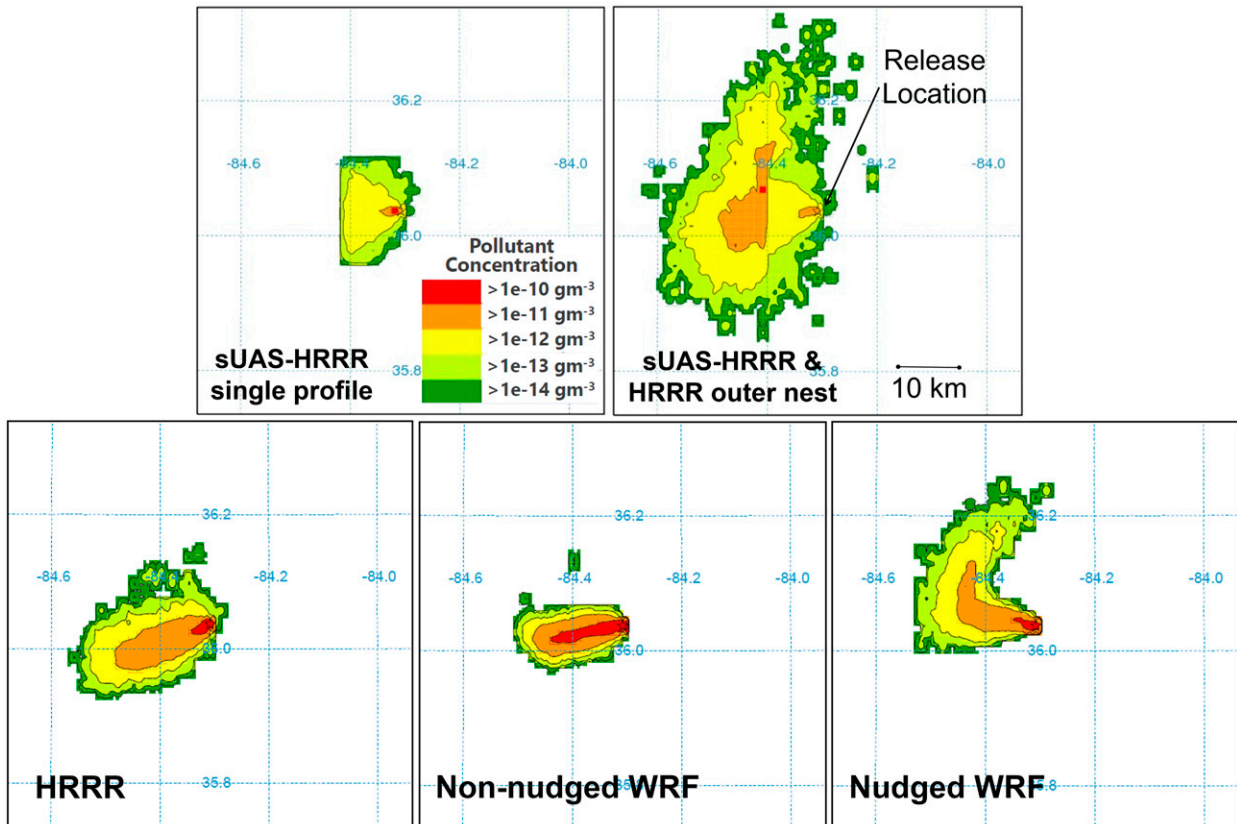


FIG. 6. Spatial plots of HYSPLIT simulations using different meteorological data at 1330 UTC 20 Aug 2020 ( $\text{g m}^{-3}$ ).

wind direction in the nonnudged and nudged simulations were similar due to the relative accuracy of the nonnudged WRF run in predicting wind direction on this day (Figs. 7 and 8). The wind speed prediction increased during the nudging period on 16 and 18 November, resulting in positive biases but decreased on 17 November, reducing the positive biases in the nonnudged case.

When we used the different meteorological inputs to drive HYSPLIT simulations, the modeled plumes on 16 November had very different spatial distributions and peak values, whereas those on 18 November appeared similar (Fig. 9). The observational nudging corrected the westerly winds in the nonnudged run to easterly winds shown in Fig. 7, resulting in the plume in the nudged simulation moving to the direction (west) opposite to the nonnudged plume (east). The plume driven by HRRR moved to the northwest but with a lower wind speed that caused it to stay closer to the release location. The overprediction of surface wind speed relative to the OSI tower observation on 16 November that is due to the sUAS nudging (Fig. 8) would likely have caused the plume to travel faster and have a lower peak concentration. On 18 November, the wind speed had a sharp increase with altitude whereas the wind direction was constant northeasterly in the lowest 500 m AGL shown in Fig. 7. Both WRF simulations predicted similar wind patterns during the sUAS profiling period on this day, yet the wind speed in the nudged WRF was slightly larger

than the nonnudged run. The relatively accurate wind in the nonnudged WRF resulted in a narrow and southwestward moving plume that the HRRR and nudged simulations also had.

c. Case 3–15 and 16 December 2021

The automated ingestion of sUAS observations was added to READY for incorporating the sUAS measurements to generate WRF meteorological fields to drive HYSPLIT simulations in a quasi-operational end-to-end system. When the sUAS files for 15 and 16 December 2021 were uploaded to the READY server, they were automatically converted to a nudging-ready format for WRF modeling. A meteorological simulation of a 3-km grid spacing domain (WRF-d3b in Fig. 2) centered at the sUAS location was initialized using forecast NAM data. The nudged WRF output were converted to HYSPLIT meteorological files, archived, and made available for users to run HYSPLIT simulations. We continue to notice that using observational nudging in WRF improves model simulated wind speed and direction toward the sUAS profiles. The change of wind direction with height was better simulated in the nudged WRF simulation than in the nonnudged WRF and HRRR, as reflected in the reduced MAE in Table 3. The MAE was computed using sUAS profiles on 15 and 16 December 2021 for temperature ( $^{\circ}\text{C}$ ), wind speed ( $\text{m s}^{-1}$ ), and wind direction ( $^{\circ}$ ). The errors between the model and sUAS-collected

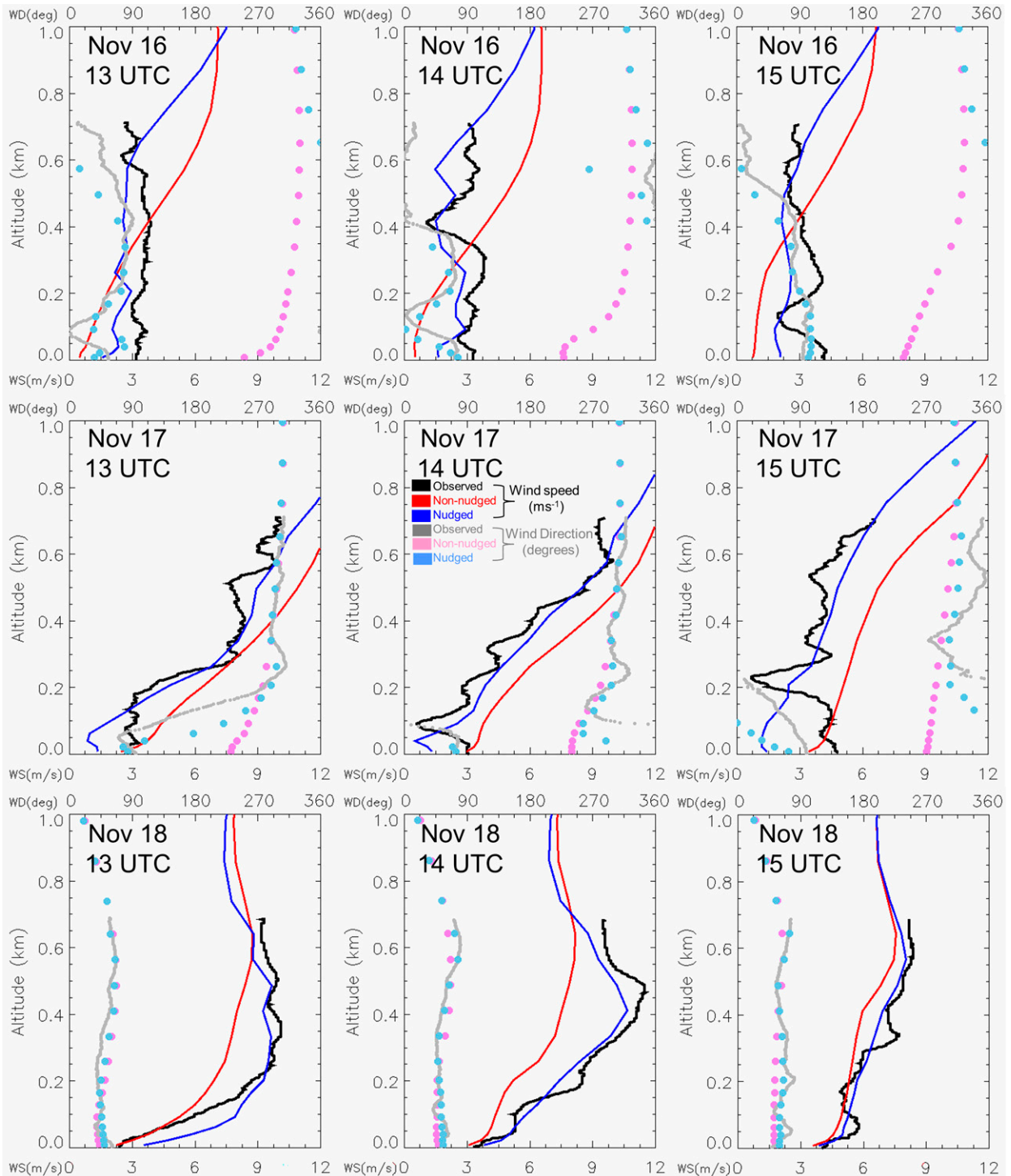


FIG. 7. The observed and WRF-modeled wind speed and direction profiles at (left) 1300, (center) 1400, and (right) 1500 UTC (top) 16, (middle) 17, and (bottom) 18 Nov 2020. The wind speed refers to the bottom axis ( $\text{m s}^{-1}$ ), and the wind direction refers to the top axis ( $^{\circ}$ ).

values for these variables were significantly reduced when observational nudging is used in the simulation.

Time series of wind profiles at OSI for nudged and non-nudged WRF simulations on 15 and 16 December 2021 are

shown in Fig. 10. WRF meteorological fields from the non-nudged and nudged runs were output every 30 min, and the first available sUAS profile was at around 1300 UTC. We observed that the wind profile difference between the nonnuded

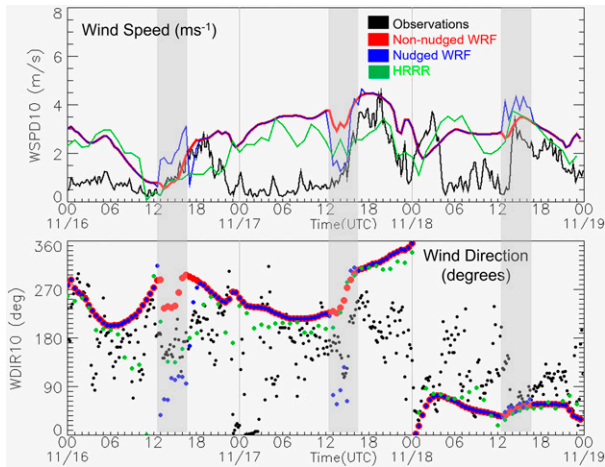


FIG. 8. Time series of observed and modeled (top) wind speed and (bottom) wind direction at OSI for 16–18 Nov 2020. The sUAS observational nudging was carried out during the gray-shaded time periods.

and nudged simulations was more prominent on the first day than on the second day (Fig. 10). On 15 December, the observational nudging with sUAS-collected data produced stronger wind speeds. The most significant differences between the nonnudged and nudged wind field occurred in the layer from

the surface to about 400 m during 1300–1500 UTC. The non-nudged WRF run simulated calm northeasterly to westerly winds [less than 2 kt ( $1 \text{ kt} \approx 0.51 \text{ m s}^{-1}$ )] for the lowest 200 m AGL. However, the sUAS observational nudging generated calm southerly winds (less than 3 kt) near the surface and a layer of southwesterly wind (4–12 kt) increasing with heights at about 100–400 m, which was above the modeled nocturnal boundary layer. The next day (16 December), the nonnudged and nudged wind profiles were very similar, except that a larger wind speed was produced by the sUAS observational nudging in the lowest 100 m above the ground. Also, a higher PBL height was simulated in the earlier morning in the nudged WRF.

We then conducted HYSPLIT simulations using three meteorological inputs: HRRR, nonnudged WRF, and nudged WRF. The concentration plots at 1400 UTC (i.e., one hour after the initiation) on 15 and 17 December 2021 are shown in the top row of Figs. 11 and 12, respectively. Note that the concentration is calculated based on the mass of computational particles in an output domain with a resolution of  $1 \text{ km} \times 1 \text{ km}$  horizontally and 0–100 m vertically. The horizontal distribution showed more significant differences between the three simulations on 15 December than on 16 December, which is consistent with the wind pattern evaluation (Fig. 10). On 15 December, the nonnudged case suggested stagnant conditions, causing the plume to stay close to the release location.

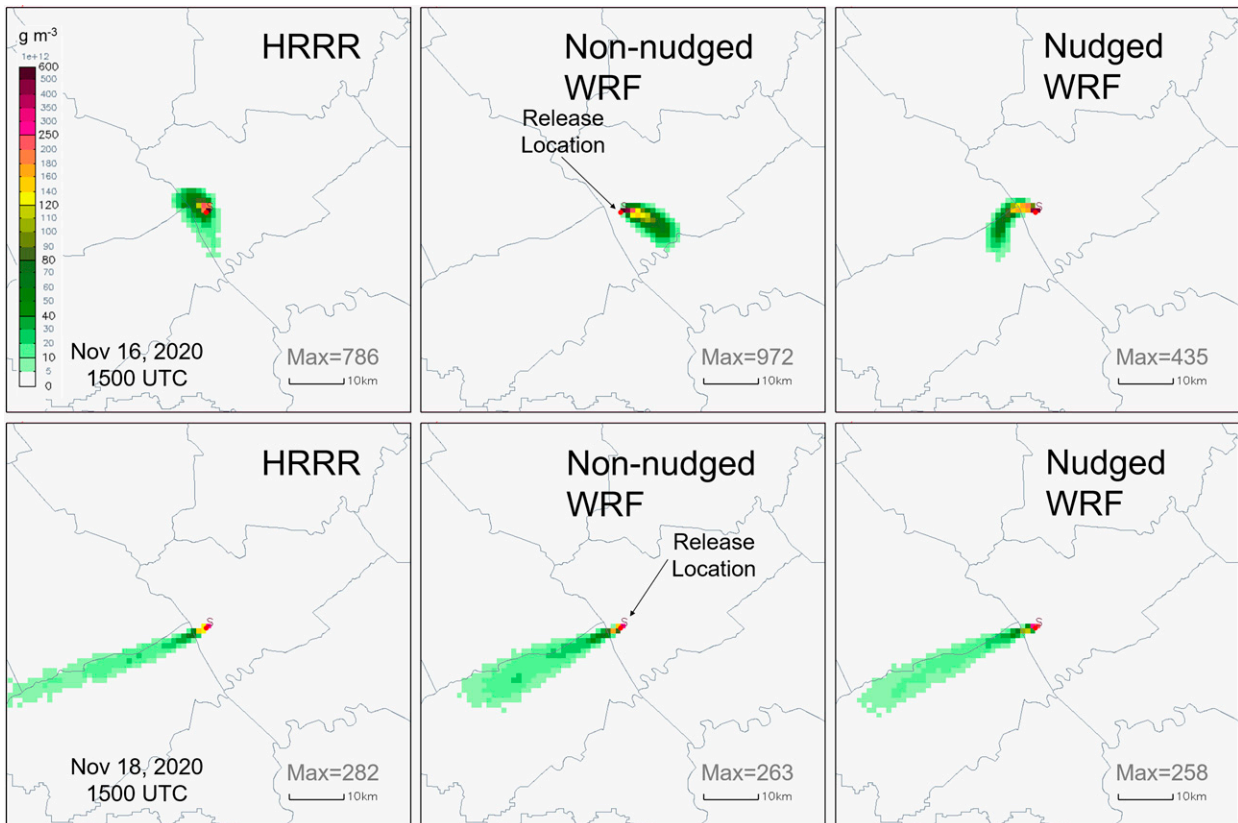


FIG. 9. Spatial plots of HYSPLIT simulations using different meteorological data at 1500 UTC (top) 16 and (bottom) 18 Nov 2020 ( $\text{g m}^{-3}$ ).



TABLE 3. MAE computed using sUAS-collected data for temperature ( $^{\circ}\text{C}$ ), wind speed ( $\text{m s}^{-1}$ ), and wind direction ( $^{\circ}$ ).

	15 Dec 2021			16 Dec 2021		
	<i>T</i>	WS	WD	<i>T</i>	WS	WD
Nonnudged WRF	2.07	2.43	40.93	1.32	2.56	19.69
Nudged WRF	1.16	0.87	11.84	0.66	1.13	11.38
HRRR	1.89	1.39	30.37	1.69	1.68	20.39

The impact of using observational nudging was more noticeable on 15 December as a high pressure system was present over the eastern United States, resulting in a relatively weak synoptic regime in the study area. On 16 December, a relatively strong influence of the synoptic scale winds was present as a result of a cold front approaching. Thus, the influence of sUAS data nudging on the WRF simulation was small.

In addition to the wind fields in the nudged WRF causing different transport patterns, particle vertical distribution figures reveal a difference in the vertical mixing of particles in HYSPLIT simulations. The bottom rows of Figs. 11 and 12 show the vertical distribution of particles. On 15 December, simulated particles in the runs using HRRR and nonnudged WRF data tended to stay near the surface (up to about 100 m, color coded as red), while in the nudged WRF, particles were

dispersed to higher altitudes. As a result, the nudged run had a lower maximum concentration at the surface level ( $768 \text{ g m}^{-3}$ ) relative to the other two runs (HRRR:  $1934 \text{ g m}^{-3}$  and non-nudged:  $4457 \text{ g m}^{-3}$ ). The next day, the simulation using the nudged WRF had particles distributed within the lowest 200 m, while the other simulations dispersed some particles to high altitudes. However, the nudged WRF and HRRR provided a similar magnitude of southwesterly wind that was obviously larger than the nonnudged wind (Fig. 10). With the adjusted wind pattern and vertical mixing characteristics, the nudged run ( $453 \text{ g m}^{-3}$ ) had a maximum surface concentration close to the HRRR case ( $589 \text{ g m}^{-3}$ ), yet much lower than the non-nudged case ( $1256 \text{ g m}^{-3}$ ).

In HYSPLIT, the advection of particles uses mean wind fields, while the dispersion calculation requires the standard deviations of turbulent velocity (Ngan et al. 2019; Stein et al. 2015). The Kantha–Clayson mixing scheme, used in this study (one of the physics configuration choices available in HYSPLIT) computes the turbulent velocity as a function of friction velocity, convective velocity scale, and boundary layer height. As a result of the adjustment of wind and temperature toward the sUAS measurements, other meteorological variables such as vertical velocity, friction velocity, and mixing height are indirectly changed. Figure 13 shows the east–west cross section of vertical velocity and horizontal wind barbs

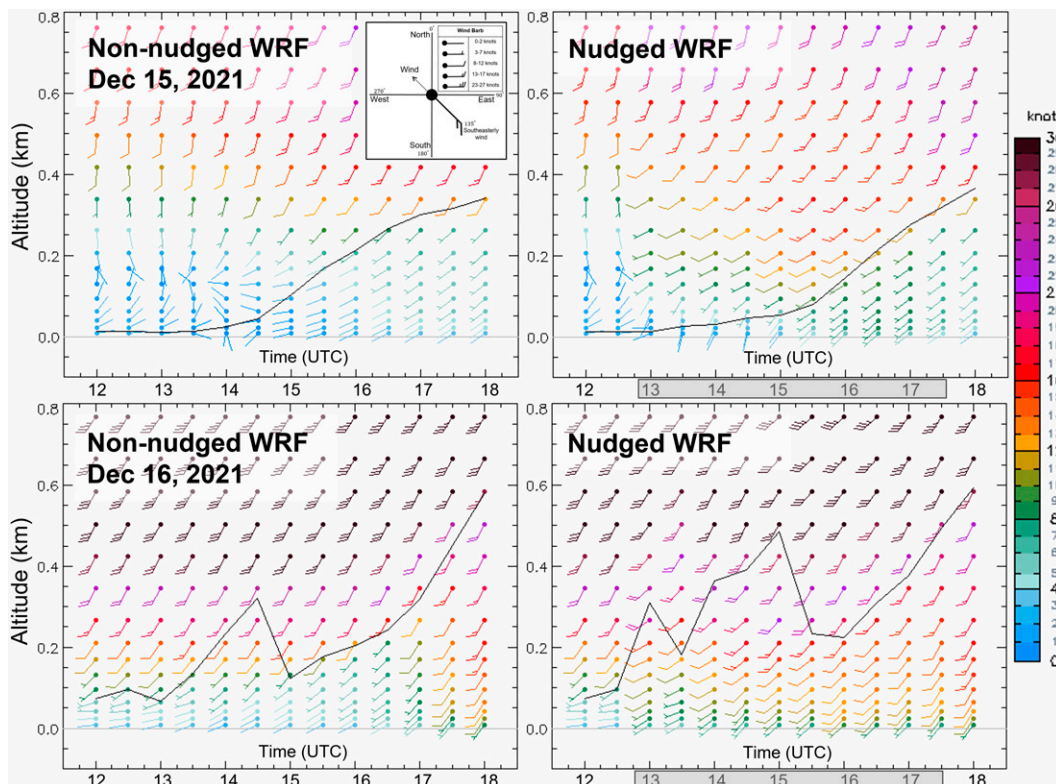


FIG. 10. Time series of wind profile plots at OSI on (top) 15 and (bottom) 16 Dec 2021 for (left) nonnudged WRF and (right) nudged WRF (kt). The x axis is time (h), and the y axis represents the altitude (km AGL). The black line is the modeled PBL height (km AGL). The sUAS observational nudging was carried out during the gray-shaded time periods.



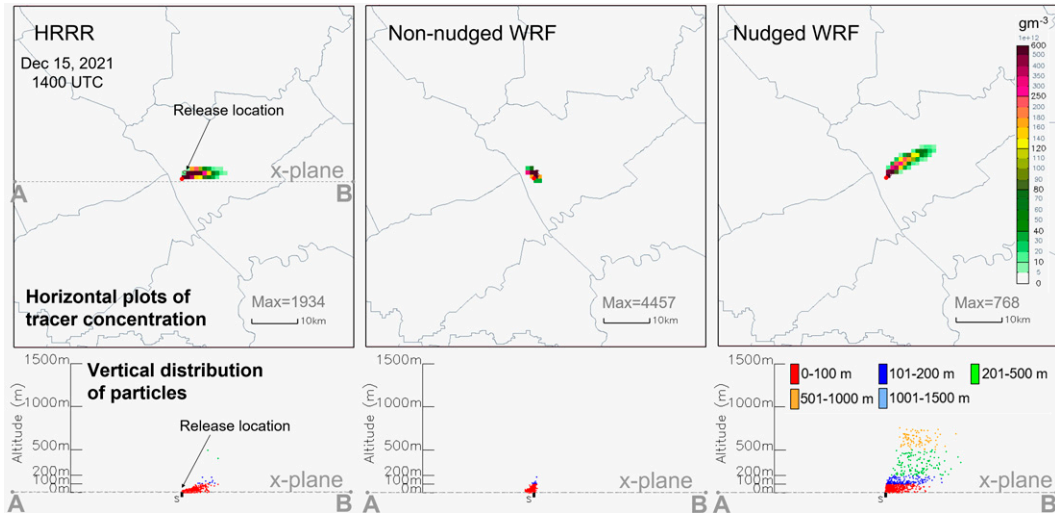


FIG. 11. HYSPLIT simulations using (left) HRRR data, (center) nonnudged WRF, and (right) nudged WRF at 1400 UTC 15 Dec 2021, showing (top) horizontal plots of tracer concentration ( $\text{g m}^{-3}$ ) and (bottom) vertical distribution of particles, with color-coded dots for different altitudes (m AGL).

from the nonnudged and nudged WRF simulations. Furthermore, using the nudged WRF meteorological data, HYSPLIT may compute different stability and mixing parameters than the nonnudged data. Figure 14 compares the profiles of the vertical velocity variance computed in HYSPLIT based on the nonnudged and nudged WRF meteorological fields. Inspection of these two figures suggests why the differences in the simulated vertical mixing. On 15 December, the nudged WRF run had a larger vertical velocity variance (Fig. 14), especially in the lowest 100 m, and had positive vertical velocity above the release location and adjacent grid cells (the second-

seventh model layer, i.e., about 23–172 m AGL) (Fig. 13), that resulted in transporting and dispersing particles more efficiently to higher altitudes than the nonnudged simulation as shown in Fig. 11. On 16 December, the nonnudged WRF had a weak vertical velocity variance near the surface and gradually increased with height, while the maximum value occurred at around 500 m. The vertical velocity variance near the surface was significantly higher in the nudged WRF than the nonnudged WRF, then decreased at about 100 m. The maximum vertical velocity variance in the nudged WRF occurred at a higher level, around 600 m. A slightly stronger downward

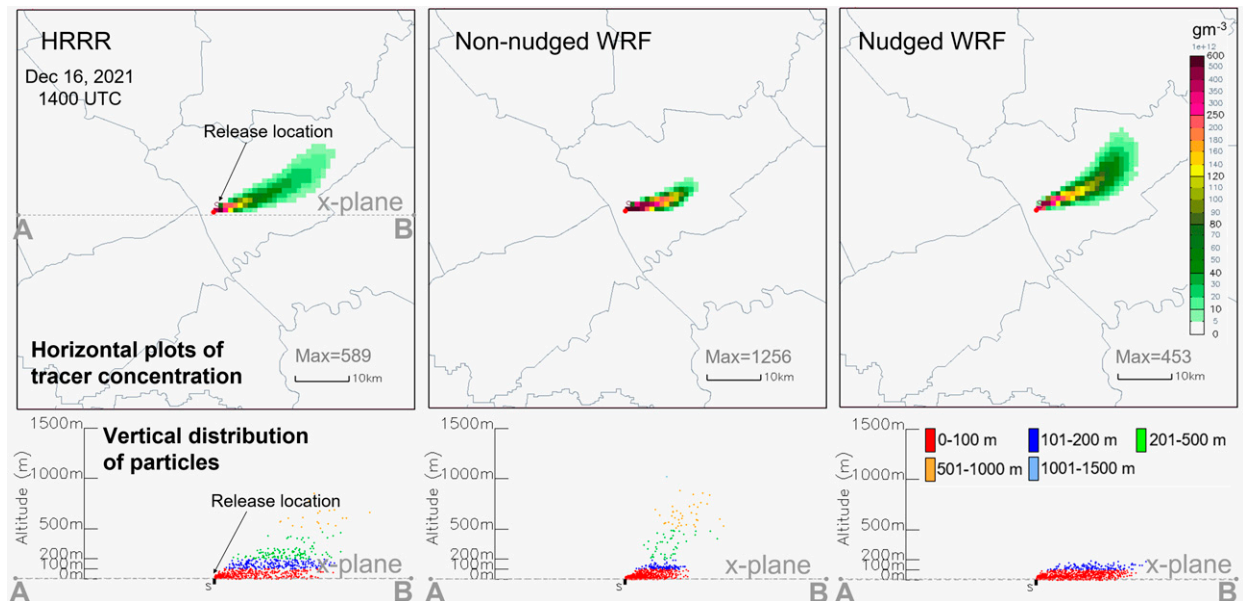


FIG. 12. As in Fig. 11, but at 1400 UTC 16 Dec 2021.

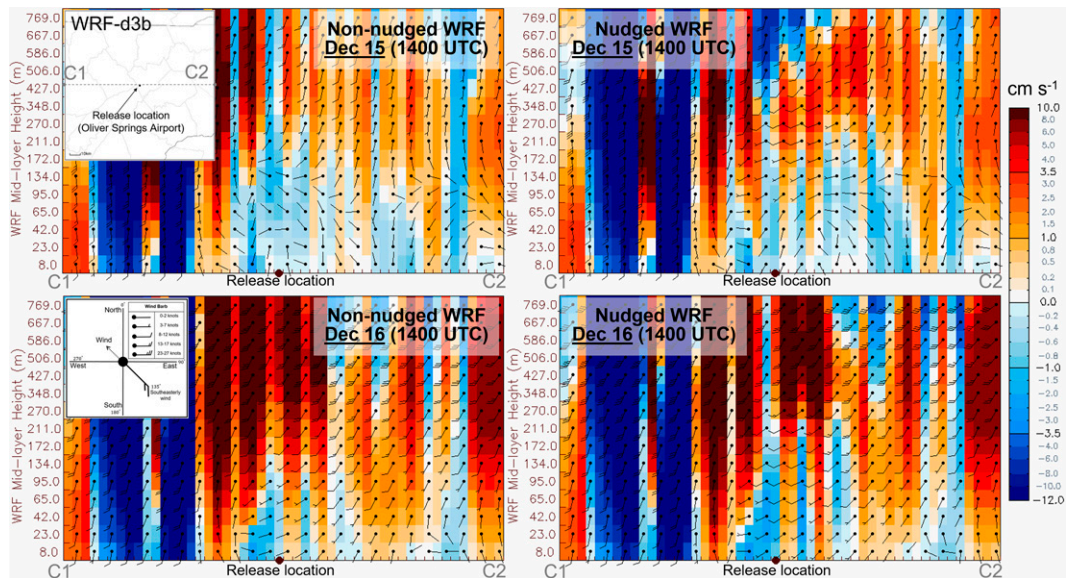


FIG. 13. The cross section (C1–C2 on the map) of vertical velocity and horizontal wind barbs from (left) nonnudged WRF and (right) nudged WRF at 1400 UTC (top) 15 and (bottom) 16 Dec 2021 ( $\text{cm s}^{-2}$ ). The black dot indicates the HYSPLIT plume release location and the sUAS profiling location.

vertical velocity above the release location (surface–eighth model layer, i.e., up to 211 m AGL) was present in the WRF run using observational nudging with sUAS profiles. As a result, the nudged plume was kept under 200 m, as shown in Fig. 12. The observational nudging of sUAS-collected data not only adjusts the prediction of state variables, such as mean wind and temperature, but also alters the conditions in the lower part of the PBL that further impact the simulated mixing used in dispersion simulations.

## 5. Summary

An sUAS was flown near Oliver Springs Airport to obtain meteorological measurements. Wind and temperature profiles with the sUAS were collected for the lowest few hundred meters AGL during the morning transition of the boundary layer. We conducted numerical experiments using WRF and HYSPLIT to better understand the feasibility and benefit of using the sUAS observations in meteorological and dispersion modeling. After converting to the HYSPLIT meteorological input files, sUAS profiles appended with upper level profiles from HRRR meteorological fields were used directly to drive HYSPLIT simulations. However, a single profile only provides a small area of gridded data for running HYSPLIT. If using an NWP product, such as the HRRR meteorological fields, for a domain outside this limited area, artificially high or low concentrations may be simulated near the domain boundary when the plume travels from the inner to outer domain due to the inconsistencies of the winds in the two meteorological products. The preferred approach is incorporating the measurements into meteorological simulations to generate more accurate, continuous input data for dispersion

modeling. In this study, the temperature and wind data obtained from the sUAS profiles were ingested into the WRF simulations through observational nudging to adjust the model toward the measurements. The profile evaluation shows that the model biases for wind and temperature were reduced in the nudged WRF simulation. The improvement of wind direction was especially evident, with up to 71% reduction of mean absolute error. In comparison with the tower measurements at OSI (at the sUAS location) and KCRC (about 12 km southeast of OSI), the observational nudging approach positively impacted the wind prediction. The inaccurate wind patterns and mixing characteristics in the WRF meteorological fields during the morning transition period of PBL are corrected by using observational nudging with sUAS measurements.

HYSPLIT simulations for a 3-h hypothetical release using a unit emission were conducted using the nudged WRF Model fields, and the results were compared with the run with nonnudged WRF. The movement of the calculated plume was impacted when using the nudged WRF data due to the model wind patterns being corrected by the sUAS observations. Furthermore, the simulated particles in the run using nudged WRF were dispersed to higher altitudes because of the adjusted mixing characteristics in the lower part of the boundary layer. The comparison of dispersion results on 15 and 16 December 2021 shows that using sUAS observational nudging is more significant under weak synoptic conditions than strong influences from regional weather (e.g., resulting from an approaching cold front). To enhance the HYSPLIT simulations on READY, we added an automated sUAS data ingestion to the system so that dispersion simulations can be driven by the meteorological data converted directly from the observations or the nudged files

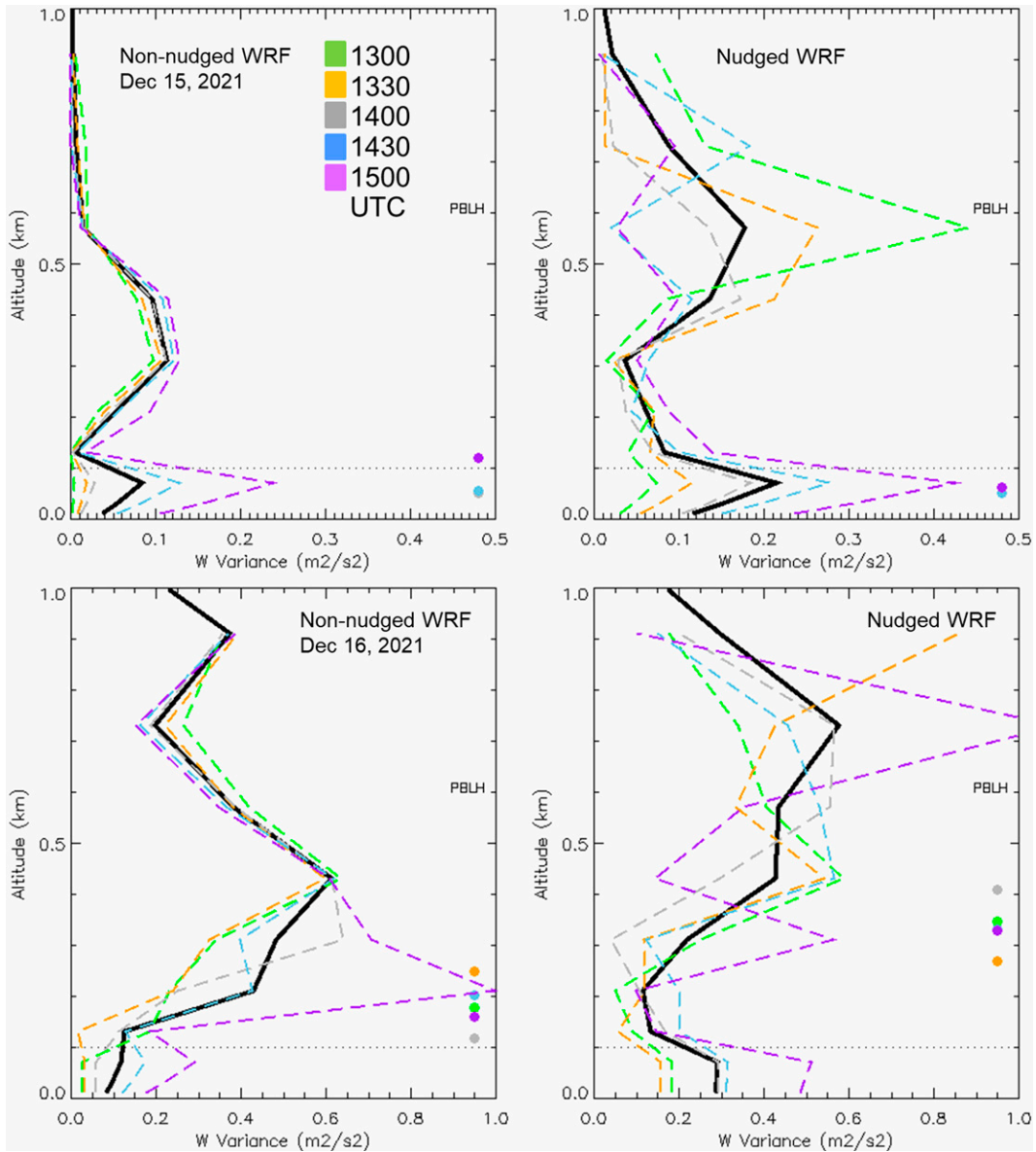


FIG. 14. The profile of vertical velocity variance from HYSPLIT at OSI on (top) 15 and (bottom) 16 Dec 2021 for (left) nonnudged WRF and (right) nudged WRF ( $m^2 s^{-2}$ ). Color-coded lines indicate different hours, and the black lines are the averaged vertical velocity variance for 1300–1500 UTC. Color-coded dots are PBL height (km AGL) at the corresponding hours.

with the sUAS measurements. This new feature can better support the local NWS WFO in Morristown for planning emergency response activities or responding to a real event involving releases of harmful materials to the air. Very different dispersion results were introduced by the meteorological fields used. The observational nudging produced not just an sUAS-nudged wind flow but also adjusted meteorological fields that further impacted the mixing calculation in HYSPLIT. Note that the dispersion simulations presented in this study were hypothetical releases, and the “true” dispersion was unknown. It will be ideal to have tracer experiments coinciding with sUAS flights that

provide passive tracer releases and well-designed sampling networks for tracer concentration. Then, by using tracer data to run dispersion simulations and evaluating the results, we may assess how the sUAS-nudged meteorological input can actually improve the dispersion results. An example of such controlled tracer experiments is Project Sagebrush phase 1 (Finn et al. 2016). Ngan et al. (2018, 2019) used sampled concentrations for known tracer releases to assess the dispersion model performance and weather data coinciding with those releases to evaluate the meteorological fields that drove the dispersion simulations. ARL’s Data Archive of Tracer Experiments and Meteorology



(DATEM; <http://www.arl.noaa.gov/DATEM.php>) includes other available tracer experiments conducted on different spatial scales and geographic locations (Rolph et al. 2017).

In future work, we plan to collect additional vertical profiles of meteorological variables taken by sUAS in different synoptic conditions and hours of the day to evaluate the likely benefit of the inclusion of sUAS observations on WRF and HYSPLIT simulations. Given increasing interest and development of sUAS technology, we will continue the work to collect data with other types of sUAS, such as fixed wing and rotary wing, and incorporate them into the WRF simulation to benefit HYSPLIT modeling. We will further study the degree of improvement in the nudged results by comparing these results with independent surface data (tower measurements) and vertical profile measurements not used in the nudging. Further, we will investigate the effects of different nudging configurations for different observational datasets. Using more sUAS observations, we will continue sensitivity tests for observational nudging and study the impact of nudged WRF meteorological fields on vertical mixing in dispersion simulations. Coupling these analyses with tracer experiments, where possible, will allow us to test whether the sUAS-adjusted dispersion simulations are more accurate, as would be expected if the underlying meteorological fields driving the simulation are more accurate.

**Acknowledgments.** This work was supported by NOAA Cooperative Institutes, Award NA19NES4320002, at the Cooperative Institute for Satellite Earth System Studies. In addition, we thank John Williams of the Oliver Springs Airport for allowing us to use the facility for our UAS profiles. We note that the results and conclusions of this study, as well as any views expressed herein, are those of the authors and do not necessarily reflect those of NOAA or the U.S. Department of Commerce.

**Data availability statement.** The UAS data are archived by the NOAA National Centers for Environmental Information (<https://doi.org/10.25921/tchq-7x60>). The OSI and KCRC tower data are available online (at <https://www.ncei.noaa.gov/archive/accession/0278335/data/0-data> and <https://www.ncei.noaa.gov/archive/accession/0277213/data/0-data>, respectively).

## REFERENCES

- Abida, R., Y. Addad, D. Francis, M. Temimi, N. Nelli, R. Fonseca, O. Nesterov, and E. Bosc, 2022: Evaluation of the performance of the WRF model in a hyper-arid environment: A sensitivity study. *Atmosphere*, **13**, 985, <https://doi.org/10.3390/atmos13060985>.
- Bailey, S. C. C., C. A. Canter, M. P. Sama, A. L. Houston, and S. W. Smith, 2019: Unmanned aerial vehicles reveal the impact of a total solar eclipse on the atmospheric surface layer. *Proc. Roy. Soc.*, **475A**, 20190212, <https://doi.org/10.1098/rspa.2019.0212>.
- Barbieri, L., and Coauthors, 2019: Intercomparison of small unmanned aircraft system (sUAS) measurements for atmospheric science during the LAPSE-RATE campaign. *Sensors*, **19**, 2179, <https://doi.org/10.3390/s19092179>.
- Bauer, H.-S., S. K. Muppa, V. Wulfmeyer, A. Behrendt, K. Warrach-Sagi, and F. Spath, 2020: Multi-nested WRF simulations for studying planetary boundary layer processes on the turbulence-permitting scale in a realistic mesoscale environment. *Tellus*, **72A**, 1761740, <https://doi.org/10.1080/16000870.2020.1761740>.
- Benjamin, S. G., and Coauthors, 2016: A North American hourly assimilation and model forecast cycle: The Rapid Refresh. *Mon. Wea. Rev.*, **144**, 1669–1694, <https://doi.org/10.1175/MWR-D-15-0242.1>.
- Buban, M. S., T. R. Lee, E. J. Dumas, C. B. Baker, and M. Heuer, 2019: Observations and numerical simulation of the effects of the 21 August 2017 North American total solar eclipse on surface conditions and atmospheric boundary-layer evolution. *Bound.-Layer Meteor.*, **171**, 257–270, <https://doi.org/10.1007/s10546-018-00421-4>.
- Butterworth, B. J., and Coauthors, 2021: Connecting land-atmosphere interactions to surface heterogeneity in CHEESEHEAD19. *Bull. Amer. Meteor. Soc.*, **102**, E421–E445, <https://doi.org/10.1175/BAMS-D-19-0346.1>.
- Chai, T., A. Stein, and F. Ngan, 2018: Weak-constraint inverse modeling using HYSPLIT-4 Lagrangian dispersion model and Cross-Appalachian Tracer Experiment (CAPTEX) observations—Effect of including model uncertainties on source term estimation. *Geosci. Model Dev.*, **11**, 5135–5148, <https://doi.org/10.5194/gmd-11-5135-2018>.
- Chen, F., and J. Dudhia, 2001: Coupling and advanced land surface-hydrology model with the Penn State-NCAR MM5 modeling system. Part I: Model implementation and sensitivity. *Mon. Wea. Rev.*, **129**, 569–585, [https://doi.org/10.1175/1520-0493\(2001\)129<0569:CAALSH>2.0.CO;2](https://doi.org/10.1175/1520-0493(2001)129<0569:CAALSH>2.0.CO;2).
- Cuchiara, G. C., and B. Rappengluck, 2019: Simulating the influence of convective decay parameterization for a case study in Houston, TX. *Atmos. Environ.*, **204**, 68–77, <https://doi.org/10.1016/j.atmosenv.2019.02.016>.
- de Boer, G., and Coauthors, 2020a: Development of community, capabilities, and understanding through unmanned aircraft-based atmospheric research: The LAPSE-RATE campaign. *Bull. Amer. Meteor. Soc.*, **101**, E684–E699, <https://doi.org/10.1175/BAMS-D-19-0050.1>.
- , and Coauthors, 2020b: Data generated during the 2018 LAPSE-RATE campaign: An introduction and overview. *Earth Syst. Sci. Data*, **12**, 3357–3366, <https://doi.org/10.5194/essd-12-3357-2020>.
- Deng, A., and Coauthors, 2009: Update on WRF-ARW end-to-end multi-scale FDDA system. *10th WRF Users Workshop*, Boulder, CO, NCAR, 1.9, <https://www2.mmm.ucar.edu/wrf/users/workshops/WS2009/abstracts/1-09.pdf>.
- Dimitrova, R., Z. Silver, T. Zsedrovits, C. M. Hocut, L. S. Leo, S. Di Sabatino, and H. J. S. Fernando, 2016: Assessment of planetary boundary-layer schemes in the weather research and forecasting mesoscale model using MATERHORN field data. *Bound.-Layer Meteor.*, **159**, 589–609, <https://doi.org/10.1007/s10546-015-0095-8>.
- Draxler, R., B. Stunder, G. Rolph, A. Stein, A. Taylor, S. Zinn, C. Loughner, and A. Crawford, 2022: HYSPLIT user's guide. NOAA Doc., 315 pp., [https://www.arl.noaa.gov/documents/reports/hysplit\\_user\\_guide.pdf](https://www.arl.noaa.gov/documents/reports/hysplit_user_guide.pdf).
- Dumas, E. J., T. R. Lee, T. J. Schuyler, M. Buban, and B. Baker, 2021: Small unmanned aircraft system (sUAS) measurements at the Oliver springs airport. NOAA Tech. Memo. OAR



- ARL-283, 22 pp., [https://www.arl.noaa.gov/wp\\_arl/wp-content/uploads/2022/01/NOAA-Tech-Memo-283-Oliver-Springs-sUAS-Flights-1.pdf](https://www.arl.noaa.gov/wp_arl/wp-content/uploads/2022/01/NOAA-Tech-Memo-283-Oliver-Springs-sUAS-Flights-1.pdf).
- Efstathiou, G. A., R. J. Beare, S. Osborne, and A. P. Lock, 2016: Grey zone simulations of the morning convective boundary layer development. *J. Geophys. Res. Atmos.*, **121**, 4769–4782, <https://doi.org/10.1002/2016JD024860>.
- Elston, J., B. Argrow, M. Stachura, D. Weibel, D. Lawrence, and D. Pope, 2015: Overview of small fixed-wing unmanned aircraft for meteorological sampling. *J. Atmos. Oceanic Technol.*, **32**, 97–115, <https://doi.org/10.1175/JTECH-D-13-00236.1>.
- Finn, D., K. L. Clawson, R. M. Eckman, H. Liu, E. S. Russell, Z. Gao, and S. Brooks, 2016: Project sagebrush: Revisiting the value of the horizontal plume spread parameter  $\sigma_y$ . *J. Appl. Meteor. Climatol.*, **55**, 1305–1322, <https://doi.org/10.1175/JAMC-D-15-0283.1>.
- Flagg, D. D., J. D. Doyle, T. R. Holt, D. P. Tyndall, and C. M. Amerault, 2018: On the impact of unmanned aerial system observations on numerical weather prediction in the coastal zone. *Mon. Wea. Rev.*, **146**, 599–622, <https://doi.org/10.1175/MWR-D-17-0028.1>.
- Grell, G. A., and D. Devenyi, 2002: A generalized approach to parameterizing convection combining ensemble and data assimilation techniques. *Geophys. Res. Lett.*, **29**, 1693, <https://doi.org/10.1029/2002GL015311>.
- Hegarty, J., and Coauthors, 2013: Evaluation of Lagrangian particle dispersion models with measurements from controlled tracer releases. *J. Appl. Meteor. Climatol.*, **52**, 2623–2637, <https://doi.org/10.1175/JAMC-D-13-0125.1>.
- Holland, G. J., and Coauthors, 2001: The aerosonde robotic aircraft: A new paradigm for environmental observations. *Bull. Amer. Meteor. Soc.*, **82**, 889–902, [https://doi.org/10.1175/1520-0477\(2001\)082<0889:TARAAN>2.3.CO;2](https://doi.org/10.1175/1520-0477(2001)082<0889:TARAAN>2.3.CO;2).
- Houston, A. L., B. Argrow, J. Elston, J. Lahowetz, E. W. Frew, and P. C. Kennedy, 2012: The Collaborative Colorado–Nebraska Unmanned Aircraft System Experiment. *Bull. Amer. Meteor. Soc.*, **93**, 39–54, <https://doi.org/10.1175/2011BAMS3073.1>.
- Iacono, M. J., J. S. Delamere, E. J. Mlawer, M. W. Shephard, S. A. Clough, and W. D. Collins, 2008: Radiative forcing by long-lived greenhouse gases: Calculations with the AER radiative transfer models. *J. Geophys. Res.*, **113**, D13103, <https://doi.org/10.1029/2008JD009944>.
- Jensen, A. A., and Coauthors, 2021: Assimilation of a coordinated fleet of uncrewed aircraft system observations in complex terrain: EnKF system design and preliminary assessment. *Mon. Wea. Rev.*, **149**, 1459–1480, <https://doi.org/10.1175/MWR-D-20-0359.1>.
- , and Coauthors, 2022: Assimilation of a coordinated fleet of uncrewed aircraft system observations in complex terrain: Observing system experiments. *Mon. Wea. Rev.*, **150**, 2737–2763, <https://doi.org/10.1175/MWR-D-22-0090.1>.
- Jia, M., X. Huang, K. Ding, Q. Liu, D. Zhou, and A. Ding, 2021: Impact of data assimilation and aerosol radiation interaction on Lagrangian particle dispersion modelling. *Atmos. Environ.*, **247**, 118179, <https://doi.org/10.1016/j.atmosenv.2020.118179>.
- Koch, S. E., M. Fengler, P. B. Chilson, K. L. Elmore, B. Argrow, D. L. Andra Jr., and T. Lindley, 2018: On the use of unmanned aircraft for sampling mesoscale phenomena in the preconvective boundary layer. *J. Atmos. Oceanic Technol.*, **35**, 2265–2288, <https://doi.org/10.1175/JTECH-D-18-0101.1>.
- Lee, T. R., M. Buban, E. Dumas, and C. B. Baker, 2017: A new technique to estimate sensible heat fluxes around micrometeorological towers using small unmanned aircraft systems. *J. Atmos. Oceanic Technol.*, **34**, 2103–2112, <https://doi.org/10.1175/JTECH-D-17-0065.1>.
- , —, —, and —, 2019: On the use of rotary-wing aircraft to sample near-surface thermodynamic fields: Results from recent field campaigns. *Sensors*, **19**, 10, <https://doi.org/10.3390/s19010010>.
- Leuenberger, D., A. Haeefe, N. Omanovic, M. Fengler, G. Martucci, B. Calpini, O. Fuhrer, and A. Rossa, 2020: Improving high-impact numerical weather prediction with lidar and drone observations. *Bull. Amer. Meteor. Soc.*, **101**, E1036–E1051, <https://doi.org/10.1175/BAMS-D-19-0119.1>.
- Li, X., Y. Choi, B. Czader, A. Roy, H. Kim, B. Lefer, and S. Pan, 2016: The impact of observation nudging on simulated meteorology and ozone concentrations during DISCOVER-AQ 2013 Texas campaign. *Atmos. Chem. Phys.*, **16**, 3127–3144, <https://doi.org/10.5194/acp-16-3127-2016>.
- Lim, K.-S. S., and S.-Y. Hong, 2010: Development of an effective double-moment cloud microphysics scheme with prognostic cloud condensation nuclei (CCN) for weather and climate models. *Mon. Wea. Rev.*, **138**, 1587–1612, <https://doi.org/10.1175/2009MWR2968.1>.
- Loughner, C. P., B. Fasoli, A. F. Stein, and J. C. Lin, 2021: Incorporating features from the Stochastic Time-Inverted Lagrangian Transport (STILT) model into the Hybrid Single-Particle Lagrangian Integrated Trajectory (HYSPPLIT) model: A unified dispersion model for time-forward and time-reversed applications. *J. Appl. Meteor. Climatol.*, **60**, 799–810, <https://doi.org/10.1175/JAMC-D-20-0158.1>.
- Lucas, D. D., M. Simpson, P. Cameron-Smith, and R. L. Baskett, 2017: Bayesian inverse modeling of the atmospheric transport and emissions of a controlled tracer release from a nuclear power plant. *Atmos. Chem. Phys.*, **17**, 13 521–13 543, <https://doi.org/10.5194/acp-17-13521-2017>.
- NCEP/NWS/NOAA/U.S. Department of Commerce, 2000: NCEP FNL operational model global tropospheric analyses, continuing from July 1999. National Center for Atmospheric Research, accessed 23 March 2021, <https://doi.org/10.5065/D6M043C6>.
- Ngan, F., and A. F. Stein, 2017: A long-term WRF meteorological archive for dispersion simulations: Application to controlled tracer experiments. *J. Appl. Meteor. Climatol.*, **56**, 2203–2220, <https://doi.org/10.1175/JAMC-D-16-0345.1>.
- , M. Cohen, W. Luke, X. Ren, and R. Draxler, 2015: Meteorological modeling using the WRF-ARW model for Grand Bay intensive studies of atmospheric mercury. *Atmosphere*, **6**, 209–233, <https://doi.org/10.3390/atmos6030209>.
- , A. Stein, D. Finn, and R. Eckman, 2018: Dispersion simulations using HYSPLIT for the sagebrush tracer experiment. *Atmos. Environ.*, **186**, 18–31, <https://doi.org/10.1016/j.atmosenv.2018.05.012>.
- , C. P. Loughner, and A. Stein, 2019: The evaluation of mixing methods in HYSPLIT using measurements from controlled tracer experiments. *Atmos. Environ.*, **219**, 117043, <https://doi.org/10.1016/j.atmosenv.2019.117043>.
- Nielsen, K. F., and D. A. Rahn, 2022: Morning transition of the boundary layer over Dallas–Fort Worth. *J. Appl. Meteor. Climatol.*, **61**, 1433–1448, <https://doi.org/10.1175/JAMC-D-21-0169.1>.
- Nolan, P. J., and Coauthors, 2018: Coordinated unmanned aircraft system (UAS) and ground-based weather measurements to predict Lagrangian coherent structures (LCSs). *Sensors*, **18**, 4448, <https://doi.org/10.3390/s18124448>.

- Powers, J. G., and Coauthors, 2017: The Weather Research and Forecasting Model: Overview, system efforts, and future directions. *Bull. Amer. Meteor. Soc.*, **98**, 1717–1737, <https://doi.org/10.1175/BAMS-D-15-00308.1>.
- Reen, B., 2016: A brief guide to observational nudging in WRF. UCAR Tech. Rep., 34 pp., <http://www2.mmm.ucar.edu/wrf/users/docs/ObsNudgingGuide.pdf>.
- Rolph, G., A. Stein, and B. Stunder, 2017: Real-time environmental applications and display system: READY. *Environ. Modell. Software*, **95**, 210–228, <https://doi.org/10.1016/j.envsoft.2017.06.025>.
- Rutledge, G. K., J. Alpert, and W. Ebisuzaki, 2006: NOMADS: A climate and weather model archive at National Oceanic and Atmospheric Administration. *Bull. Amer. Meteor. Soc.*, **87**, 327–342, <https://doi.org/10.1175/BAMS-87-3-327>.
- Shin, H. H., and S.-Y. Hong, 2015: Representation of the subgrid-scale turbulent transport in convective boundary layers at gray-zone resolutions. *Mon. Wea. Rev.*, **143**, 250–271, <https://doi.org/10.1175/MWR-D-14-00116.1>.
- Stein, A. F., R. R. Draxler, G. D. Rolph, B. J. B. Stunder, M. D. Cohen, and F. Ngan, 2015: NOAA's HYSPLIT atmospheric transport and dispersion modeling system. *Bull. Amer. Meteor. Soc.*, **96**, 2059–2077, <https://doi.org/10.1175/BAMS-D-14-00110.1>.
- Tomasi, E., and Coauthors, 2019: Turbulence parameterizations for dispersion in sub-kilometer horizontally non-homogeneous flows. *Atmos. Res.*, **228**, 122–136, <https://doi.org/10.1016/j.atmosres.2019.05.018>.
- Tran, T., H. Tran, M. Mansfield, S. Lyman, and E. Crosman, 2018: Four dimensional data assimilation (FDDA) impacts on WRF performance in simulating inversion layer structure and distributions of CMAQ-simulated winter ozone concentrations in Uintah Basin. *Atmos. Environ.*, **177**, 75–92, <https://doi.org/10.1016/j.atmosenv.2018.01.012>.
- Wagner, T. J., P. M. Klein, and D. D. Turner, 2019: A new generation of ground-based mobile platforms for active and passive profiling of the boundary layer. *Bull. Amer. Meteor. Soc.*, **100**, 137–153, <https://doi.org/10.1175/BAMS-D-17-0165.1>.
- Wildmann, N., G. A. Rau, and J. Bange, 2015: Observations of the early morning boundary-layer transition with small remotely-piloted aircraft. *Bound.-Layer Meteor.*, **157**, 345–373, <https://doi.org/10.1007/s10546-015-0059-z>.
- Wulfmeyer, V., and Coauthors, 2018: A new research approach for observing and characterizing land–atmosphere feedback. *Bull. Amer. Meteor. Soc.*, **99**, 1639–1667, <https://doi.org/10.1175/BAMS-D-17-0009.1>.
- , J. M. Valencia Pineda, S. Otte, M. Karlbauer, M. V. Butz, T. R. Lee, and V. Rajtschan, 2023: Estimation of the surface fluxes for heat and momentum in unstable conditions with machine learning and similarity approaches for the LAPE data set. *Bound.-Layer Meteor.*, **186**, 337–371, <https://doi.org/10.1007/s10546-022-00761-2>.